Stabilization of Au Monatomic-High Islands on the (2×2)-N_{ad} Reconstructed Surface of Wurtzite AlN(0001)

Benoit Eydoux,[1,2] Bulent Baris,[1] Hassan Khoussa,[1,3] Olivier Guillermet,[1,2]
Sébastien Gauthier,[1] Xavier Bouju,[1] and David Martrou[1,*]

[1]*Centre d'élaboration de matériaux et d'études structurales, CEMES-CNRS, UPR 8011,
Nanosciences Group, 29 rue Jeanne Marvig, F-31055 Toulouse, France*
[2]*Université Toulouse III, UPS, 118 route de Narbonne, F-31062 Toulouse, France*
[3]*Laboratoire LSMC, Université d'Oran 1 Ahmed Ben Bella, 31100 Oran, Algeria*

Noncontact atomic force microscopy images show that gold grows on the (2×2)-N_{ad} reconstructed polar (0001) surface of AlN insulating films, in the form of large monatomic islands. High-resolution images and *in situ* reflection high-energy electron diffraction spectra reveal two moiré patterns from which an atomic model can be built. Density functional theory calculations confirm this model and give insight into the mechanisms that lead to the stabilization of the monolayer. Gold adsorption is accompanied, first, by a global vertical charge transfer from the AlN substrate that fulfills the electrostatic stability criterion for a polar material, and second, by lateral charge transfers that are driven by the local chemical properties of the (2×2)-N_{ad} reconstruction. These results present alternative strategies to grow metal electrodes onto nitride compounds with a better controlled interface, a crucial issue for applications.

I. INTRODUCTION

Heterostructures made with AlN and GaN nitride compounds are at the basis of numerous devices in optoelectronics such as deep ultraviolet ($\sim$210 nm) light-emitting or laser diodes [1,2], in high-power and high-frequency electronics with high electron mobility transistors (HEMT) [3,4], in solid-state quantum information [5,6], and in micro- and nanoelectromechanical systems owing to their piezoelectric properties for bulk acoustic wave devices [7,8]. An important prerequisite is that these devices must be powered in an optimal way with good electrical contacts. It is known that usual technological processes such as growing metallic electrodes after NO_2 pretreatment, create a lot of defects at the interface between the nitride layers and the metallic electrodes. These defects deteriorate dramatically the charge injection with apparition of transient effects [9–11]. For HEMTs these defects can also induce trap charges at the metal-semiconductor interface that degrade the conduction of the source and drain ohmic contacts (see Ref. [12] and references within). The control of these interfaces is thus important to gain in reproducibility and in reliability of the active devices.

The AlN compound is also a good candidate in the molecular electronics research frame. Indeed, its large direct band gap of 6.2 eV [13,14] combined with the possibility to control its surface at the atomic level by molecular beam epitaxy (MBE) make it a good insulating substrate to fabricate molecular devices based on single molecules. However, such single molecules have to be contacted to metallic nanoelectrodes, which should be two-dimensional (2D) islands with less than two monatomic layers in height to allow imaging the connected object with an atomic force microscope (AFM). These 2D islands are able to play the role of charge reservoirs or intermediate electrodes to be contacted by the tips of a multiprobe ultrahigh vacuum (UHV) instrument [15–17].

For these two applications, the actual challenge is thus to grow epitaxially 2D metallic electrodes at the surface of AlN or GaN. Pezzagna *et al.* showed in 2008 that Mg can grow layer by layer at the surface of GaN(0001) [18]. We reproduce this growth at the surface of AlN(0001), but due to the reactivity of the Mg atoms, the layer does not stay metallic after a few days in UHV [19]. Nevertheless, this result shows that the metal growth mechanisms are quite comparable between the GaN(0001) and the AlN(0001) surfaces, which present reconstructions with the same atomic structure [20,21]. Because of the large gap of AlN, the physics of metal growth is related to the growth of a metallic structure on an insulating substrate. Most metals grow in the form of three-dimensional (3D) clusters at the early stages of their deposition on insulating substrates [22]. This situation generally results from the unfavorable surface and interface free-energy balance involved in the formation of two-dimensional (2D) islands.

It was reported recently that the charge state of a metallic aggregate on an insulating substrate can have a determining influence on the morphology of the metal clusters. For Au nanoclusters on MgO(001) films supported by a metallic substrate, a dimensionality crossover from 2D growth for

*Corresponding author.
dmartrou@cemes.fr

thin-enough MgO films to 3D growth for thicker films was predicted [23] and observed [24]. The calculation shows that for thin MgO films a negative charge is transferred from the metal substrate towards the interface between the Au clusters and the oxide. The electrostatic contribution of this extra-charge layer increases the adhesion energy, hence favoring the 2D growth. The amount of charge transfer is determined by the efficiency of electron tunneling through the insulating film, which is strongly suppressed for large thicknesses. Another possibility to promote the growth of 2D clusters with the same electrostatic mechanism is to use a suitably doped bulk insulating material to provide the necessary extra charges. This strategy was proposed for Au on MgO(001) [25] and confirmed experimentally for Au on CaO thick films doped with Mo ions [26].

A third proposition to induce 2D growth stabilized by charge transfer is to use a polar substrate with a stoichiometric surface. Indeed, polar materials have a natively charged surface to fulfill the electrostatic stability criterion [27,28]. The use of these charged surfaces in the presence of metals to stabilize polar-oxide substrates has been suggested by calculations for a long time [23,29–32]. But some recent experimental works show only 3D growth of metal islands on polar MgO(111) nanosheets [33].

Here, we show that the use of the polar $2H$-AlN(0001) (2×2)-N_{ad} reconstructed surface allows the growth of an epitaxially gold monatomic layer, following a fourth stabilization route. In contrast to the previous charging routes, this one has the advantage for highlighting the specific application mentioned previously of preserving the insulating character of the substrate.

Compared with polar oxides, nitride compounds are ionocovalent and offer the possibility to incorporate atoms to stabilize reconstructed surfaces. We recently elaborated and characterized AlN(0001) thick films, whose surface is polar. We identified the mechanism of charge compensation for one of its (2×2) reconstructions [34]: According to the (2×2)-N_{ad}, the surface charge is mostly localized on one extra N adatom per (2×2) surface unit cell, satisfying quantitatively the electrostatic stability criterion predicted by classical electrostatic theory [27]. Other recent calculations confirmed the stability of the AlN(0001)(2×2)-N_{ad} reconstruction [35]. This nonstoichiometric surface also presents donor and acceptor sites that are prone to create new bonds with metallic atoms [36].

In the following, we first present the experimental methods and the results obtained using reflection high-energy electron diffraction (RHEED) and noncontact (NC) atomic force microscopy (AFM). Structural models of the system based on the (2×2)-N_{ad} reconstructed and on the bulk-truncated AlN(0001) surface are then proposed as starting points for density functional theory (DFT) calculations. The DFT energies indicate that the Au layer is preferably adsorbed on the (2×2)-N_{ad} reconstructed surface, which is confirmed by comparing the Au atomic positions extracted from experimental NC AFM images at

low temperature (4 K) and those from DFT calculations. As expected, some Au atoms create bonds with the donor and acceptor sites of the (2×2) N_{ad}, inducing inhomogeneous charge transfer on the gold layer and in the gold layer. It is then discussed how these new bonds and charge transfer can explain the stabilization mechanism of the Au monatomic layer.

II. EXPERIMENTS

The growth of AlN samples is carried out in a MBE chamber equipped with a RHEED gun working at 15 keV. AlN films with a thickness between 100 and 150 nm are grown on $4H$-SiC(0001) substrates in the presence of 2×10^{-5} Torr of NH_3 and under an Al flux at a substrate temperature of $990 \pm 30\,°C$ [37]. The experimental conditions needed to stabilize the $(2 \times 2)\,N_{ad}$ reconstruction are discussed in Ref. [34]. After the formation of the $(2 \times 2)\,N_{ad}$ reconstructed surface, the substrate temperature is decreased to $500\,°C$ and gold is deposited with a beam equivalent pressure of 5×10^{-9} Torr during one to two minutes. The RHEED diagram acquired during the Au growth in Fig. 1(a) displays one of the AlN[$2\,1\,\bar{3}\,0$] streaks (in blue), characteristic of the AlN(0001) surface, as well as new streaks associated with the gold deposit, which will be discussed later. When the AlN (2×2)-N_{ad} reconstructed surface is covered with at least 1 monolayer (ML) of gold, twofold streaks are no more visible in the RHEED pattern, meaning that the (2×2) periodicity disappears. NC AFM experiments are conducted with a room temperature (RT) UHV NC AFM (Scienta Omicron Nanotechnology GmbH,
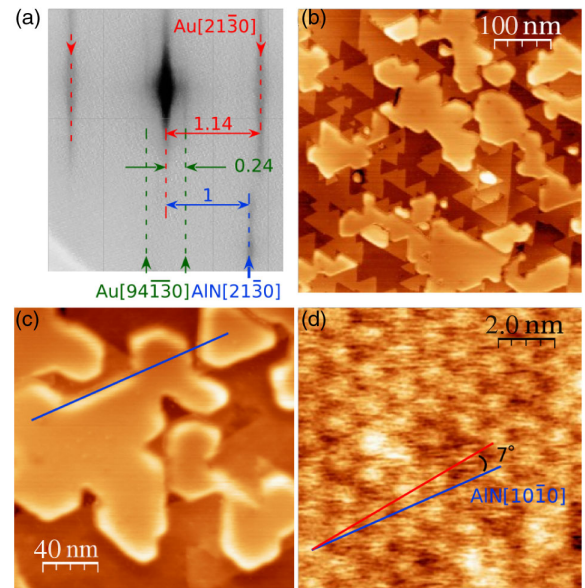
FIG. 1.　(a) Reconstructed RHEED pattern obtained during the growth of Au (see text for explanations). (b) Room temperature NC AFM image of ~0.5-ML Au deposit. (c) Au island on which (d) is obtained. (d) High-resolution NC AFM image of the Au monolayer.

Taunusstein, Germany) belonging to the same UHV setup as the MBE chamber [15,16]. We used silicon cantilevers (NanoSensors PPP-QNCHR) with resonance frequencies between 280 and 300 kHz and quality factors between 32 000 and 40 000. The oscillation amplitude is stabilized at 5 nm.

The NC AFM image presented in Fig. 1(b) is obtained on a 100-nm-thick AlN film, on which approximately 0.5 ML of gold is deposited. Under these conditions no tunneling current can be detected through the sample in the $[-10$ V, 10 V] accessible bias range, confirming the truly insulating character of the AlN substrate. The AlN surface is characterized by triangular terraces limited by $\langle 10\bar{1}0 \rangle$-oriented step edges [34,37]. The Au deposit appears as large disconnected islands around 3-Å high, indicating a monatomic thickness. They are limited by rounded corners and linear borders aligned on the AlN(0001) step edges. A higher-resolution image obtained on the Au island of Fig. 1(c) is displayed in Fig. 1(d). It shows a hexagonal structure with a periodicity of 13 ± 1 Å rotated by $7° \pm 1°$ from the AlN$[1\,0\,\bar{1}\,0]$ direction. It is not possible to get a better resolution at RT. For this reason, the sample is transferred to a low temperature (LT) UHV NC AFM ($T = 5$ K) (Scienta Omicron Nanotechnology GmbH, Taunusstein, Germany), using a UHV transfer chariot with a base pressure in the low 10^{-10} Torr range. A tuning fork in the qPlus configuration is used with a glued Pt-Ir tip. The quality factor is $Q = 78\,000$ and the amplitude is $A = 1$ nm. As shown in Fig. 2(a), a quasihexagonal array of black dots can be observed at 5 K with an average nearest-neighbor (NN) distance of 2.8 ± 0.1 Å. This distance is close to the NN distance of 2.88 Å in bulk gold, indicating that this array corresponds to a Au monolayer. Here, gold atoms appear as depressions on the image. Such a contrast inversion is common in NC AFM images [38,39]. It results from an interplay between short- and long-range tip-substrate forces that makes the frequency shift vs distance curves crossing at different altitudes depending on the tip position above the surface unit cell [40]. The image in Fig. 2(a) also exhibits a larger-scale periodic height modulation with an amplitude of approximately 0.2 Å that can be associated with a moiré pattern ($M1$). The maxima observed in the topography are positioned on a hexagonal lattice of parameter 12.6 ± 0.5 Å, rotated relative to the AlN$[1\,0\,\bar{1}\,0]$ direction by an angle of $8.8 \pm 1°$. These values are consistent with the apparent moiré observed at RT in Fig. 1(d), indicating that the same structure $M1$ is imaged in both cases. Moreover, a closer look at the image in Fig. 2(a) shows that the unit cell describing the Au monolayer structure is in fact larger than the apparent moiré observed at RT: The atomic arrangement is different from one maximum to the other. There are in fact three different atomic structures (hexagon, triangle pointing up, and triangle pointing down), as illustrated in the green color in Fig. 2(a). Positioning its origin at the center of a hexagon gives the unit cell drawn with green lines in Fig. 2(a).
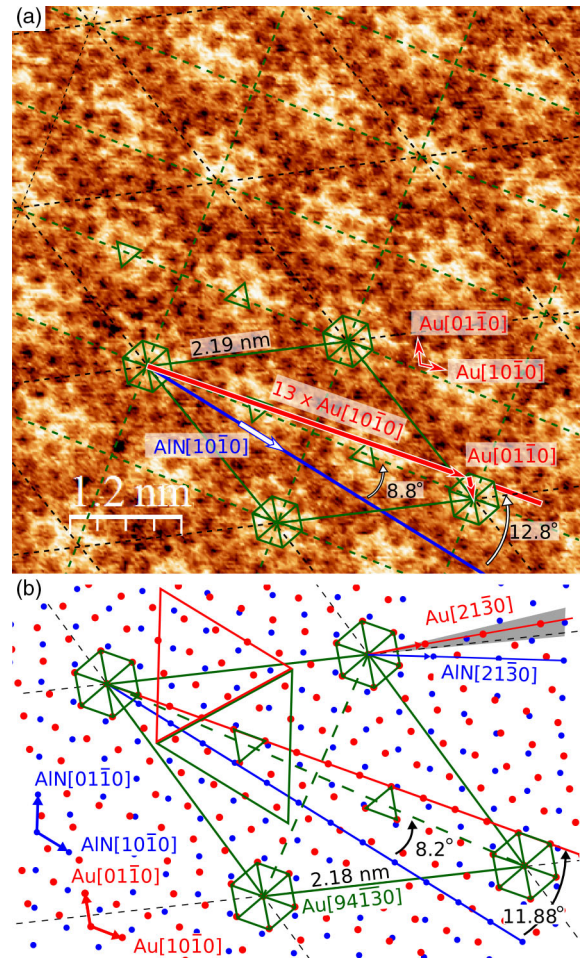
FIG. 2. (a) Low-temperature (5 K) NC AFM image of Au/AlN(0001). (b) Corresponding unrelaxed model with red and blue hexagonal lattices representing the Au layer and the Al atoms of the AlN(0001) surface, respectively. The $[1\,0\,\bar{1}\,0]$ direction of AlN and Au are colored in blue and red, respectively. The supercell of the moiré pattern is represented by green lines. The shaded area in (b) corresponds to the angular domain covered by the reconstructed RHEED pattern. The position of the cell (called dft1t) used for calculations is depicted with red and green triangles.

The structural model shown in Fig. 2(b) is built by (a) Orienting the image in Fig 2(a) relative to the AlN substrate using the $\langle 1\,0\,\bar{1}\,0 \rangle$ oriented steps of the bare surface. The angle of the Au hexagonal layer relative to the Al hexagonal lattice of the AlN surface, which corresponds in Fig. 2(a) to the angle between the red line (Au$[1\,0\,\bar{1}\,0]$ direction) and the blue line (AlN$[1\,0\,\bar{1}\,0]$ direction) is measured at $12.8 \pm 1.5°$ in the counterclockwise direction.

(b) Positioning the Au layer such that the central atom of a green hexagon coincides with an Al atom of the AlN surface to respect the local hexagonal symmetry.

The parameters describing the Au layer unit cell are refined by applying the geometrical relations between the Au hexagonal layer and the Al hexagonal network of

TABLE I. Epitaxial relations and cell parameters for the $M1$ superstructure. The dft1t and dft1h models have the same dimensions as the apparent moiré.

Name		Epitaxial relation	$a = b$ (Å)	α (deg)	AlN(1×1) unit cell	Au atoms	$d_{\text{Au-in plane}}$ (Å)
M1	Supercell	Au$[9\,4\,\overline{13}\,0]\|AlN[8\,5\,\overline{13}\,0]$	21.8	11.88	49	61	2.79
	Apparent moiré	$\frac{1}{3}$(Au$[13\,\overline{1}\,\overline{12}\,0])\|\frac{1}{3}$(AlN$[13\,2\,\overline{15}\,0])$	12.5	8.21	16.33	20.33	
dft1t and dft1h models		Au$[4\,\overline{1}\,\overline{3}\,0]\|AlN[4\,0\,\overline{4}\,0]$	12.52	10.89	16	21	2.73

the AlN surface [36]. The results are presented in Table I. The cell parameter and angle are now 21.8 Å and 11.88°, very close to the experimental values of 21.9 ± 1 Å and $12.8° \pm 1.5°$. The mean NN Au in-plane distance in the layer is 2.79 Å. But, as observed in the image in Fig. 2(a), the layer is slightly distorted meaning that the NN distance fluctuates around this value. This model is in full agreement with the RHEED diagram displayed in Fig. 1(a). This diagram is built by summation of RHEED images within the angular domain represented by the shaded area in Fig. 2(b), that includes the Au$[2\,1\,\overline{3}\,0]$ direction of the hexagonal Au atomic structure (in red) and the Au$[9\,4\,\overline{13}\,0]$ direction of the moiré (in green). Considering that the distance from the origin of the AlN$[2\,1\,\overline{3}\,0]$ streak in the RHEED diagram is inversely proportional to $a_{\text{AlN}}\sqrt{3}$, the real-space periodicity in the corresponding direction, it is straightforward to calculate the mean NN distance in the Au layer a_{Au} from $a_{\text{AlN}}\sqrt{3}/a_{\text{Au}}\sqrt{3} = 1.14 \pm 0.03$, giving $a_{\text{Au}} = 2.73 \pm 0.1$ Å and d_{Au}, the lattice parameter of the moiré from $a_{\text{AlN}}\sqrt{3}/d_{\text{Au}} = 0.24 \pm 0.01$, giving $d_{\text{Au}} = 22.4 \pm 1$ Å. These values are fully compatible with the experimental and calculated values reported in the preceding paragraphs.

Another moiré pattern ($M2$) is identified by LT NC AFM imaging on the same sample. The images display local Au hexagonal and triangular configurations that are very similar to what is observed with $M1$ [36]. They are associated, in the models presented in Fig. 2(b) in this work and Fig. 2(b) in the Supplemental Material [36], with local in-plane matching between Au and Al atoms. $M2$ is analyzed using the same method as discussed here and the corresponding data are presented in Ref. [36]. This observation suggests that the moiré patterns could be built with three (nine) of these atomic arrangements in $M1$ ($M2$).

The structural model in Fig. 2(b) is built by considering only the hexagonal network constituted by the surface Al atoms of the AlN substrate. The latter should cover an integer number of AlN(2×2) unit cells and there are 49 AlN(1×1) units in $M1$ (Table I). Thus, the actual supercell should be at least four times larger than the green cell in Fig. 2. However, as suggested by the RHEED observations and confirmed by the calculations that will be presented in the next part, the initial structure of the (2×2)-N$_{\text{ad}}$

reconstruction of the AlN substrate is strongly modified under the Au adlayer, leading to the disappearance of the (2×2) periodicity.

III. FIRST-PRINCIPLES CALCULATIONS

To unravel the origin of the stabilization of the gold monolayer on AlN(0001), we perform DFT calculations using the Vienna *ab initio* simulation package (VASP) [41–43], with the plane-wave basis set expanded with a cutoff of 500 eV using the projector-augmented wave method (PAW) [44]. A k-point mesh of $(3 \times 3 \times 1)$ is set for the electronic convergence. The Perdew-Burke-Ernzerhof exchange and correlation functional is used thanks to its efficiency to predict surface geometries [45]. The unit cell of the Au monolayer in the $M1$ configuration determined previously is too large to tackle DFT calculations. It is then necessary to choose a reduced unit cell, which can, nevertheless, grasp the essential physics governing the adsorption of the Au monolayer on AlN$(0001)(2 \times 2)$-N$_{\text{ad}}$.

We choose a unit cell that includes four AlN(2×2) unit cells called dft1t model, whose size and orientation are close to those of the apparent unit cell observed in Fig. 2(b). The unit cell of the dft1t model presents the triangle coincidence between Au and Al atoms. We build also another dft1h model where the hexagonal coincidence between Au and Al atoms is visible [36]. The characteristics of the dft1t and dft1h models are summarized in Table I. The DFT slab includes 233 atoms, arranged in six bilayers of (4×4) unit cells of wurtzite AlN terminated by the four additional N atoms of the (2×2)-N$_{\text{ad}}$ with 21 Au atoms on top resulting in a high Au coverage of $\Theta = 21/16 = 1.31$. The back side of the slab is passivated by pseudohydrogen atoms with a $0.75 |e|$ charge [46,47]. The atomic structure is optimized until forces between atoms remain below 10^{-3} eV Å^{-1}. The evaluation of the atomic partial charges is performed by a real-space partitioning Bader analysis with a fine grid spacing of 0.016 Å [48].

The obtained energies for the dft1t and dft1h models are very close, with a difference of 37 meV. They present a similar behavior regarding the interactions between Au atoms and AlN surface [36], and in the following we will focus on the optimized structure of the dft1t model
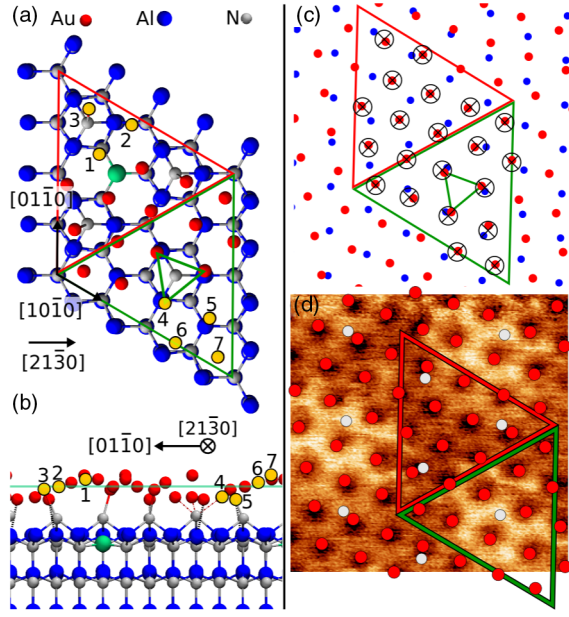
FIG. 3. (a) Top view of the optimized structure of the dft1t model. The cell is divided into two regions depicted by a green and a red triangle. (b) Projection along the $[2\,1\,\bar{3}\,0]$ axis helps us to visualize the different heights of gold atoms with respect to the mean Au plane. Gold atoms are numbered as explained in the text. (c) Comparison of the dft1t model with the unrelaxed model in Fig. 2(b). Cross-centered circles correspond to the relaxed positions of Au atoms in dft1t model. (d) Adjustment of the Au atoms' calculated positions on the NC AFM image of $M1$. The white dots indicate the position of the N_{ad} atoms.

presented in Figs. 3(a) and 3(b). Thanks to the two threefold-symmetry axes of the hexagonal unit cell, only 7 Au atoms over 21 in the unit cell are inequivalent. They are named $Au^{(n)}$ with $n = \{1, 7\}$. One member of each of these seven classes is colored in yellow in Fig. 3. For the sake of the discussion, the unit cell is divided into two parts depicted by a red (R) and a green (G) triangle.

Table II presents the NN distances between the Au atoms in the calculated structure. They range from 2.67 to 3.15 Å with a mean value of 2.82 Å close to the 2.88 Å bulk Au value. The largest distance of 3.15 Å corresponds to the distance between the $Au^{(4)}$ atoms that form a triangle in the

green half of the unit cell [Fig. 3(a)], and is also very close to the lattice parameter of the calculated AlN bulk unit cell. Apart from a small rotation, the $Au^{(4)}$ triangle matches perfectly the aluminum lattice of the AlN surface. We use this observation to position the calculated unit cell on the model in Fig. 2(b) by superimposing the triangle formed by the $Au^{(4)}$ atoms to the left green triangle of the model. As illustrated in Fig. 3(c), the in-plane position of the Au atoms in the calculated structure (crossed circles) is quite close to those of the unit cell (red circles) drawn in Fig. 2(b). Their differences reflect the distortion of the Au layer with respect to the perfect hexagonal lattice of the model in Fig. 2(b). Each laterally displaced Au atom reveals a distortion of the hexagonal layer that suggests a strong local interaction with the substrate. The most displaced atoms are $Au^{(4)}$, as remarked previously, but also $Au^{(5)}$ and $Au^{(3)}$. A comparison of the calculated Au positions with the NC AFM atomic-resolution image of the moiré in Fig. 3(d) results, indeed, in a fair agreement [36]. These results justify our choice for the DFT unit cell and show that it can provide a realistic local description of the Au layer.

The anomalous length of the Au bonds in the green triangle and their matching with the underlying Al atoms of the surface is a clear indication of a strong Au-Al interaction. An examination of the vertical positions and Bader charges of the Au atoms presented in Table III confirms this observation. In G, $Au^{(5)}$ atoms are 0.82 Å below the mean plane of the Au layer with a charge of $-0.48\,|e|$. They are nearly on top of aluminum atoms named b-Al that are in a sp^2 configuration on the initial (2×2)-N_{ad} reconstruction [36]. The bond formation between $Au^{(5)}$ and b-Al atoms is revealed by the switch of the b-Al hybridization from the nearly planar sp^2 observed on the (2×2)-N_{ad} to the nearly tetrahedral sp^3 configuration after gold deposit. The $Au^{(4)}$ atoms are 0.68 Å down and have a smaller charge of $-0.13\,|e|$. They are also on top of the Al atoms that are linked to one N_{ad} atom. The interaction between $Au^{(4)}$ and this N_{ad} atom is revealed by the decrease of $-0.8\,|e|$ of its charge compared to its initial (2×2)-N_{ad} value. This induces a weakening of the strength of the $Al-N_{ad}$ bond as shown by the increase of its length from 1.9 to 2.17 Å, resulting to an upward

TABLE II. Bond lengths $d_{Au^{(i)}-Au^{(j)}} \pm 0.005$ Å between the seven different atoms.

Au$^{(i)}$ \ Au$^{(j)}$	1	2	3	4	5	6	7
1		2.76	2.73	2.93			2.74
2	2.73		2.81	2.67	2.98		
3	2.93	2.81			2.76	2.76	2.79
4		2.67		3.15	2.90	2.71	
5		2.98	2.76	2.90		2.82	2.92
6	2.74		2.76	2.71	2.82		2.79
7			2.79		2.92	2.79	2.79

TABLE III. Bader charges and height differences from the mean plane of Au among the seven classes of atom.

Triangle	Au$^{(i)}$	Δz (Å)	$(|e|)$	Bond length (Å)
Red	1	0.53	−0.03	
	2	0.04	−0.09	
	3	−0.17	0.1	2.13 (N_{ad})
Green	4	−0.68	−0.13	2.58 (Al), 2.2 (N_{ad})
	5	−0.82	−0.48	2.61 (b-Al)
	6	0.30	−0.05	
	7	0.79	−0.08	

displacement of 0.18 Å of this N_{ad}. $Au^{(3)}$ is the only positively charged atom with 0.1 $|e|$ and is the closest to N_{ad} in R. Note also that the b-Al atoms represented in green and close to this N_{ad} stays in the sp^2 configuration, meaning that it has no interaction with Au atoms. The other Au atoms of the structure remain almost neutral.

The interactions between gold atoms and the AlN (2×2)-N_{ad} surface strongly modify the original position of the N_{ad} and b-Al atoms, inducing the disappearance of the (2×2) periodicity in accordance with the RHEED observations. Another way to explain this disappearance would be based on the removal of the N_{ad} atoms. To assess this point, we perform DFT calculations on both Au hexagonal and triangle configurations above the unreconstructed AlN(0001) and find that their energy is 1.5 eV per (1×1) cell larger than the model based on the (2×2)-N_{ad} reconstruction [36]. Additionally, the dispersion of the $d_{Au\text{-in plane}}$ bond lengths is 0.017 Å, that is 13 times lower than the value measured from the image in Fig. 1(d) [36]. This small dispersion means that the Au layer is close to a perfect hexagonal structure unlike what is observed experimentally. These results indicate that the models based on the (2×2)-N_{ad} structure are the most relevant to explain our experimental results.

The Bader charges in the dft1t model are averaged plane by plane and compared with the system without Au atoms. The values of σ_S at the ith bilayer in Table IV is the cumulative sum starting from the Au layer

$$\sigma_S^{(i)} = \frac{1}{n^2} \sum_{j=0}^{i} \tilde{q}_{B_j},$$

where n is the number of (1×1) unit cells. These calculations are both performed with six bilayers of AlN(0001).

The addition of the gold atomic layer induces an upward transfer of the surface charge density leading to an average charge of -0.11 $|e|$ per Au atom or -0.1425 $|e|/S$, approximately 24% of the compensating surface charge density σ_S. We suggest that this charge explains at least partially the 2D growth mode of Au on AlN(0001)(2×2)-N_{ad}, as for Au on MgO thin films or on Mo-doped CaO [26]. In addition, the

electrostatic criterion is fulfilled. Note that this criterion does not depend on the reconstruction or the structure of the metal deposit, thus, the surface charge σ_S in Au/AlN(2×2)-N_{ad} is the same as the one on the AlN(2×2)-N_{ad}. Only the surface dipole differs between them.

Upon deposition of Au atoms on the (2×2)-N_{ad}, the space group of the system changes from $p3m1$ to $p3$ allowing the two triangles G and R to be considered as independent. In the DFT cell without Au, this separation results in three b-Al acceptor sites in G and one in R. Reversely, three N_{ad} donor sites take place in R and one in G. This difference of symmetry suggests that the charge reorganization occurs laterally.

To verify it, charge redistribution is evaluated as the difference between the sum of the charge densities calculated for the separated Au layer (n_{Au}) and for the AlN substrate (n_{AlN}) frozen in their final atomic structure and the charge density of the final system. δn represents the valence charge-density difference and $\delta \tilde{n}$ is the total (valence and core) charge-density difference. Negative (positive) values account for a depletion (an excess) in the electronic density. Figure 4(a) shows the total charge-density differences of both red and green triangles along the $[0\,0\,0\,1]$ direction. Integration along z over the red (green) curves indicates a charge of $-3|e|$ $(+3|e|)$.
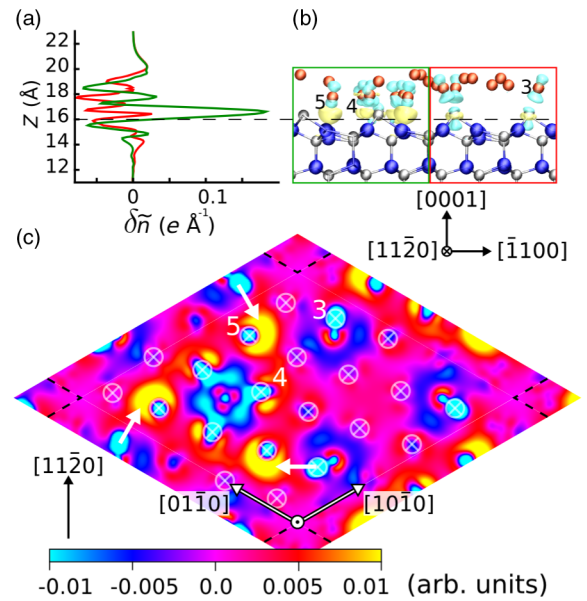
FIG. 4. (a) Lateral average of the total electronic density difference $\delta \tilde{n}(z)$ along $[0\,0\,0\,1]$ in R and G in the dft1t model. (b) Valence charge-density differences projected along the $[1\,1\,\bar{2}\,0]$. Depletion and excess in charge density with respect to $\delta n(z)$ at $(-) + 0.05|e|$ are colored, respectively, in blue and yellow. (c) Valence charge displacement integrated along z from $z = 16$ Å to the vacuum. White arrows indicate the direction of the charge transfer. Crossed circles denote the position of Au atoms. $Au^{(3)}$, $Au^{(4)}$, and $Au^{(5)}$ are indicated.

TABLE IV. Average Bader charges ($\tilde{q}_B$), surface charge (σ_S) and percentages of the theoretical surface charge calculated at Au, N_{top}, and the ith AlN bilayer (AlN$_i$) in $|e|/S$.

	AlN (2×2)-N_{ad}			Au/AlN		
	$\tilde{q}_B$	σ_S	σ_S/σ_S^{th}	$\tilde{q}_B$	σ_S	σ_S/σ_S^{th}
Au				-0.11	-0.144	24.4%
N_{ad}	-2.18	-0.545	92.1%	-1.73	-0.577	97.4%
Al_1	2.31			2.33		
N_1	-2.35	-0.582	98.3%	-2.34	-0.588	99.3%
Al_2	2.36			2.37		
N_2	-2.37	-0.589	99.5%	-2.37	-0.590	99.6%

As shown in Figs. 4(b) and 4(c), the valence charge density is globally depleted in the red triangle and accumulated in the green one. This excess charge upon Au adsorption suggests that Au atoms benefit from reactive Al and b-Al sites to stabilize the monolayer. As confirmed in the valence-charge-density displacement map in Fig. 4(b), the electron excess (yellow) is localized between $Au^{(5)}$ and b-Al atoms, and to a lesser extent between $Au^{(4)}$ and Al atoms. This effect is not present in R. Figure 4(c) shows that all N_{ad} are depleted. The depletion around the single N_{ad} in G shows a Al-N_{ad} bond weakening. The proximity of the depleted $Au^{(3)}$ and the negatively charged $Au^{(5)}$ along with their underlying b-Al atoms suggests that it is the main lateral charge-transfer mechanism. The direction of this transfer is depicted by a white arrow in Fig. 4(c).

The present case of a nonstoichiometric reconstructed surface shows an inhomogeneous electronic localization due to the Au—Al and Au—N_{ad} bond formations that strengthened the adhesion. This bond-formation mechanism is reinforced by the calculated bond lengths: $Au^{(5)}$—b-Al $= 2.58\,\text{Å}$, $Au^{(4)}$—Al $= 2.61\,\text{Å}$, $Au^{(4)}$—$N_{ad} = 2.2\,\text{Å}$, and $Au^{(3)}$—$N_{ad} = 2.13\,\text{Å}$. This effect is different from what is observed in systems such as Au nanocluster adsorbed on stoichiometric surfaces like MgO(111) [23,33] and Al-doped MgO(001) [25], where only homogeneous electronic localization at the interface is shown without bond formation.

IV. CONCLUSION

RHEED spectra and LT NC AFM images demonstrate that Au grows on AlN(0001) (2×2)-N_{ad} as large (>100 nm) monolayer islands that form moiré patterns under the influence of the substrate. These experimental data allow us to build atomic models of these structures that are used as input for first-principles DFT calculations. The overall picture that emerges from these calculations is that the hexagonal Au adlayer interacts locally with the substrate via its acceptor and donor sites. These interactions lead to local distortions of the hexagonal layer. Au adsorption is accompanied (i) by a global vertical charge transfer from the AlN substrate, that fulfills the electrostatic stability criterion for a polar surface, and (ii) by lateral charge transfers mediated by the reaction of Au with the acceptor and the donor sites of the polar substrate. The stabilization of the monolayer is the consequence of these two mechanisms that lead to energy gains of electrostatic and chemical origin. This study rationalizes the physico-chemical effects associated with the adsorption of metallic islands on a polar substrate with a nonstoichiometric reconstructed surface and opens routes for the fabrication of metallic pads particularly interesting in the context of molecular electronics. These 2D metallic pads can also be the seeds for the growth of thick 2D gold electrodes. Such electrodes with a controlled metal-semiconductor interface could improve the reliability of the nitride active devices.

[1] Y. Taniyasu and M. Kasu, Origin of exciton emissions from an AlN p-n junction light-emitting diode, Appl. Phys. Lett. **98,** 131910 (2011).

[2] S. Zhao, A. T. Connie, M. H. T. Dastjerdi, X. H. Kong, Q. Wang, M. Djavid, S. Sadaf, X. D. Liu, I. Shih, H. Guo, and Z. Mi, Aluminum nitride nanowire light emitting diodes: Breaking the fundamental bottleneck of deep ultraviolet light sources, Sci. Rep. **5,** 8332 (2015).

[3] M. Gonschorek, J.-F. Carlin, E. Feltin, M. A. Py, and N. Grandjean, High electron mobility lattice-matched AlInN/ GaN field-effect transistor heterostructures, Appl. Phys. Lett. **89,** 062106 (2006).

[4] G. Li, B. Song, S. Ganguly, M. Zhu, R. Wang, X. Yan, J. Verma, V. Protasenko, H. G. Xing, and D. Jena, Two-dimensional electron gases in strained quantum wells for AlN/GaN/AlN double heterostructure field-effect transistors on AlN, Appl. Phys. Lett. **104,** 193506 (2014).

[5] J. R. Weber, W. F. Koehl, J. B. Varley, A. Janotti, B. B. Buckley, C. G. Van de Walle, and D. D. Awschalom, Quantum computing with defects, Proc. Natl. Acad. Sci. U.S.A. **107,** 8513 (2010).

[6] J. B. Varley, A. Janotti, and C. G. Van de Walle, Defects in AlN as candidates for solid-state qubits, Phys. Rev. B **93,** 161201(R) (2016).

[7] H. P. Loebl, M. Klee, C. Metzmacher, W. Brand, R. Milsom, and P. Lok, Piezoelectric thin AlN films for bulk acoustic wave (BAW) resonators, Mater. Chem. Phys. **79,** 143 (2003).

[8] S. C. Masmanidis, R. B. Karabalin, I. De Vlaminck, G. Borghs, M. R. Freeman, and M. L. Roukes, Multifunctional nanomechanical systems via tunably coupled piezoelectric actuation, Science **317,** 780 (2007).

[9] O. Lazăr, J. G. Tartarin, B. Lambert, C. Moreau, and J. L. Roux, Correlation between transient evolutions of the gate and drain currents in AlGaN/GaN technologies, Microelectron. Reliab. **55,** 1714 (2015).

[10] S. D. Nsele, L. Escotte, J.-G. Tartarin, S. Piotrowicz, and S. L. Delage, Broadband frequency dispersion small-signal modeling of the output conductance and transconductance in AlInN/GaN HEMTs, IEEE Trans. Electron Devices **60,** 1372 (2013).

[11] S. D. Nsele, J.-G. Tartarin, L. Escotte, S. Piotrowicz, and S. Delage, InAlN/GaN HEMT Technology for Robust HF Receivers: an Overview of the HF and LF Noise Performances, in *Proceedings of the International Conference on Noise and Fluctuations (ICNF), New York, USA, 2015* (IEEE, Xi'an, 2015).

[12] H. Sánchez-Martín, Ó. García-Pérez, S. Pérez, P. Altuntas, V. Hoel, S. Rennesson, Y. Cordier, T. González, J. Mateos, and I Íñiguez-de-la-Torre, Anomalous DC and RF behavior of virgin AlGaN/AlN/GaN HEMTs, Semicond. Sci. Technol. **32**, 035011 (2017).

[13] S. Strite and H. Morkoç, GaN, AlN, and InN: A review, J. Vac. Sci. Technol. B **10**, 1237 (1992).

[14] J. Li, K. B. Nam, M. L. Nakarmi, J. Y. Lin, H. X. Jiang, P. Carrier, and S.-H. Wei, Band structure and fundamental optical transitions in wurtzite AlN, Appl. Phys. Lett. **83**, 5163 (2003).

[15] C. Joachim, D. Martrou, M. Rezeq, C. Troadec, D. Jie, N. Chandrasekhar, and S. Gauthier, Multiple atomic scale solid surface interconnects for atom circuits and molecule logic gates, J. Phys. Condens. Matter **22**, 084025 (2010).

[16] D. Martrou, L. Guiraud, R. Laloo, B. Pecassou, P. Abeilhou, O. Guillermet, E. Dujardin, S. Gauthier, J. Polesel-Maris, M. Venegas, A. Hinault, A. Bodin, F. Chaumeton, A. Piednoir, H. Guo, and T. Leoni, in *Atomic Scale Interconnection Machines: Proceedings of the 1st AtMol European Workshop Singapore, 2011* (Springer, Heidelberg, 2012), p. 35.

[17] J. Yang, D. Sordes, M. Kolmer, D. Martrou, and C. Joachim, Imaging, single atom contact and single atom manipulations at low temperature using the new ScientaOmicron LT-UHV-4 STM, Eur. Phys. J. Appl. Phys. **73**, 10702 (2016).

[18] S. Pezzagna, S. Vézian, J. Brault, and J. Massies, Layer-by-layer epitaxial growth of Mg on GaN(0001), Appl. Phys. Lett. **92**, 233111 (2008).

[19] H. Khoussa, B. Baris, M. Alchaar, F. Chaumeton, M. Ghamnia, S. Gauthier, and D. Martrou, Study of Mg, Ag, In and Au growth on AlN(0001) by NC-AFM and KPFM (to be published).

[20] C. G. Van de Walle and J. Neugebauer, First-Principles Surface Phase Diagram for Hydrogen on GaN Surfaces, Phys. Rev. Lett. **88**, 066103 (2002).

[21] T. Akiyama, D. Obara, K. Nakamura, and T. Ito, Reconstructions on AlN polar surfaces under hydrogen rich conditions, Jpn. J. Appl. Phys. **51**, 018001 (2012).

[22] C. R. Henry, Surface studies of supported model catalysts, Surf. Sci. Rep. **31**, 231 (1998).

[23] D. Ricci, A. Bongiorno, G. Pacchioni, and U. Landman, Bonding Trends and Dimensionality Crossover of Gold Nanoclusters on Metal-Supported MgO Thin Films, Phys. Rev. Lett. **97**, 036106 (2006).

[24] M. Sterrer, T. Risse, U. Martinez Pozzoni, L. Giordano, M. Heyde, H.-P. Rust, G. Pacchioni, and H.-J. Freund, Control of the Charge State of Metal Atoms on Thin MgO Films, Phys. Rev. Lett. **98**, 096107 (2007).

[25] N. Mammen, S. Narasimhan, and S. de Gironcoli, Tuning the morphology of gold clusters by substrate doping, J. Am. Chem. Soc. **133**, 2801 (2011).

[26] Y. Cui, C. Stiehler, N. Nilius, and H.-J. Freund, Probing the electronic properties and charge state of gold nanoparticles on ultrathin MgO versus thick doped CaO films, Phys. Rev. B **92**, 075444 (2015).

[27] C. Noguera, Polar oxide surfaces, J. Phys. Condens. Matter **12**, R367 (2000).

[28] J. Goniakowski, F. Finocchi, and C. Noguera, Polarity of oxide surfaces and nanostructures, Rep. Prog. Phys. **71**, 016501 (2008).

[29] V. G. Zavodinsky, M. A. Kuz'menko, and A. Kiejna, Ab initio simulation of copper and silver adsorption on the MgO (111) surface, Surf. Sci. **589**, 114 (2005).

[30] R. Benedek, Adhesive energy and charge transfer for MgO/Cu heterophase interfaces, Phys. Rev. B **54**, 7697 (1996).

[31] J. Goniakowski, Characteristics of Pd deposition on the MgO(111) surface, Phys. Rev. B **60**, 16120 (1999).

[32] J. Goniakowski and C. Noguera, Microscopic mechanisms of stabilization of polar oxide surfaces: Transition metals on the MgO(111) surface, Phys. Rev. B **66**, 085417 (2002).

[33] Z. Li, C. V. Ciobanu, J. Hu, J.-P. Palomares-Báez, J.-L. Rodríguez-López, and R. Richards, Experimental and DFT studies of gold nanoparticles supported on MgO(111) nanosheets and their catalytic activity, Phys. Chem. Chem. Phys. **13**, 2582 (2011).

[34] F. Chaumeton, R. Robles, M. Pruneda, N. Lorente, B. Eydoux, X. Bouju, S. Gauthier, and D. Martrou, Noncontact atomic force microscopy and density functional theory studies of the (2×2) reconstructions of the polar AlN(0001) surface, Phys. Rev. B **94**, 165305 (2016).

[35] P. Strak, K. Sakowski, P. Kempisty, and S. Krukowski, Structural and electronic properties of AlN(0001) surface under partial N coverage as determined by ab initio approach, J. Appl. Phys. **118**, 095705 (2015).

[36] See Supplemental Material at http://link.aps.org/supplemental/10.1103/PhysRevApplied.8.044002 for details on AlN(0001)(2×2)-N_{ad} reconstructed surface, epitaxial relations, the $M2$ moiré, a comparison of the DFT calculated Au positions with the image in Fig. 3(d), and Bader charges.

[37] F. Chaumeton, S. Gauthier, and D. Martrou, In-situ NC-AFM measurements of high quality AlN(0001) layers grown at low growth rate on $4H$-SiC(0001) and Si(111) substrates using ammonia molecular beam epitaxy, AIP Adv. **5**, 067108 (2015).

[38] F. Castanié, L. Nony, S. Gauthier, and X. Bouju, Graphite, graphene on SiC, and graphene nanoribbons: Calculated images with a numerical FM-AFM, Beilstein J. Nanotechnol. **3**, 301 (2012).

[39] O. E. Dagdeviren, J. Götzen, E. I. Altman, and U. D. Schwarz, Exploring site-specific chemical interactions at surfaces: A case study on highly ordered pyrolytic graphite, Nanotechnology **27**, 485708 (2016).

[40] M. Ondráček, C. González, and P. Jelínek, Reversal of atomic contrast in scanning probe microscopy on (111) metal surfaces, J. Phys. Condens. Matter **24**, 084003 (2012).

[41] G. Kresse and J. Furthmüller, Efficiency of ab-initio total energy calculations for metals and semiconductors using a plane-wave basis set, Comput. Mater. Sci. **6**, 15 (1996).

[42] G. Kresse and J. Furthmüller, Efficient iterative schemes for ab-initio total-energy calculations using a plane-wave basis set, Phys. Rev. B **54**, 11169 (1996).

[43] G. Kresse and D. Joubert, From ultrasoft pseudopotentials to the projector augmented-wave method, Phys. Rev. B **59**, 1758 (1999).

[44] P. E. Blöchl, Projector augmented-wave method, Phys. Rev. B **50**, 17953 (1994).

[45] J. P. Perdew, K. Burke, and M. Ernzerhof, Generalized Gradient Approximation Made Simple, Phys. Rev. Lett. **77,** 3865 (1996).

[46] K. Shiraishi, A new slab model approach for electronic structure calculation of polar semiconductor surface, J. Phys. Soc. Jpn. **59,** 3455 (1990).

[47] J. Li and L.-W. Wang, Band-structure-corrected local density approximation study of semiconductor quantum dots and wires, Phys. Rev. B **72,** 125325 (2005).

[48] G. Henkelman, A. Arnaldsson, and H. Jónsson, A fast and robust algorithm for Bader decomposition of charge density, Comput. Mater. Sci. **36,** 354 (2006).